PCCP

How Machine Learning Can Extend Electroanalytical Measurements Beyond Analytical Interpretation

Journal:	*Physical Chemistry Chemical Physics*
Manuscript ID	CP-ART-09-2023-004628.R1
Article Type:	Paper
Date Submitted by the Author:	28-Nov-2023
Complete List of Authors:	Mistry, Aashutosh; Argonne National Laboratory, Chemical Sciences & Engineering Johnson, Ian; Argonne National Laboratory Cabana, Jordi; University of Illinois at Chicago, Department of Chemistry Ingram, Brian; Argonne National Laboratory, Chemical Sciences and Engineering Srinivasan, Venkat; Argonne National Laboratory,

How Machine Learning Can Extend Electroanalytical Measurements Beyond Analytical Interpretation

Aashutosh Mistry,[1,2,a,*,†] Ian D. Johnson,[1,2,b] Jordi Cabana,[2,3,c] Brian J. Ingram,[1,2,d,*] and Venkat Srinivasan,[1,2,e,*]

[1] Chemical Sciences and Engineering Division, Argonne National Laboratory, Lemont, Illinois 60439, United States
[2] Joint Center for Energy Storage Research, Argonne National Laboratory, Lemont, Illinois 60439, United States
[3] Department of Chemistry, University of Illinois at Chicago, Chicago, Illinois 60607, United States

ABSTRACT Electroanalytical measurements are routinely used to estimate material properties exhibiting current and voltage signatures. Analysis of such measurements relies on analytical expressions of material properties to describe the experiments. The need for analytical expressions limits the experiments that can be used to measure properties as well as the properties that can be estimated from a given experiment. Such analytical relations are essentially solutions of the physics-based differential equations (with properties as coefficients) describing the material behavior under certain specific conditions. In recent years, a new machine learning-based approach has been gaining popularity wherein the differential equations are numerically solved to interpret the electroanalytical experiments in terms of corresponding material properties. Since the physics-based differential equations are solved, one can additionally estimate underlying fields, e.g., concentration profile, using such an approach. To exemplify the characteristics of such a Machine Learning assisted interpretation of electroanalytical measurements, we use data from the Hebb-Wagner test on a magnesium spinel intercalation host. As compared to the traditional analytical expression-based interpretation, the emerging approach decreases experimental efforts to characterize relevant material properties as well as provides field information that was previously inaccessible.

[*] Corresponding authors: aashutosh.mistry@mines.edu (AM) ingram@anl.gov (BJI) vsrinivasan@anl.gov (VS)
[†] Present address: Department of Mechanical Engineering, Colorado School of Mines, Golden, Colorado 80401, United States
[a] ORCID: 0000 – 0002 – 4359 – 4975
[b] ORCID: 0000 – 0001 – 5491 – 9627
[c] ORCID: 0000 – 0002 – 2353 – 5986
[d] ORCID: 0000 – 0002 – 5219 – 7517
[e] ORCID: 0000 – 0002 – 1248 – 5952

INTRODUCTION

Electroanalytical techniques are instrumental to understanding material behavior in complex electrochemical systems[1,2]. Electrochemical systems function based on interrelated behavior of multiple materials. Electroanalytical techniques, in principle, characterize each of the relevant physicochemical behaviors of these materials, e.g., conductivity of electrolytes, reaction rates at electrode/electrolyte interfaces, and diffusion in intercalation hosts. As we envision new electrochemical systems to meet societal needs, we have to search for corresponding materials. In this context, electroanalytical techniques are quite valuable as one can screen materials based on their measured properties instead of having to build electrochemical systems and screen materials based on observed system behavior. With this motivation, in recent years, machine learning techniques have been employed to accelerate materials screening by automating electroanalytical experiments[3,4]. While rapid screening of properties that are quick to measure is conceptually straightforward, e.g., conductivity, many properties require long experiments. Additionally, one may have to carry out multiple electroanalytical experiments to characterize each of the relevant properties. For example, transport in battery electrolytes is characterized by two thermodynamic properties – density and thermodynamics factor – and three transport properties – conductivity, diffusivity, and transference number. Each of these requires a different experiment with thermodynamic factor, diffusivity, and transference number experiments spanning hours to days[5–15].

The need for individual experiments is a characteristic aspect of electroanalytical tests. Since such tests are interpreted by curve fitting analytical equations, the experiments have to be devised such that the underlying physics equations afford an analytical solution. For example, the electrolyte diffusivity is typically measured using a restricted diffusion experiment[6] that ensures that only concentration gradient-driven ion transport is dominant. Alternatively, transference number measurements using potentiostatic hold have to approach a steady state wherein only the ion of interest is mobile[5,16] (prior to the steady state, all the solution-based species are mobile which in turn negates an analytical solution[17]).

Instead, if we solve for the full physics computationally, we can utilize the full electrochemical experiment (at the expense of an analytical solution). Some recent studies exploring such an alternate interpretation are documented in **Table 1**. In the absence of an analytical solution, estimation of the corresponding material properties does become computationally involved. Herein, machine learning techniques, e.g., Bayesian Optimization, can reduce the computational burden[18]. Such implementations of Bayesian Optimization differ from computational[19–21] or experimental screening[3,4] of materials. We herein discuss Bayesian Optimization-based approaches to estimating material properties. In the subsequent discussion, we first illustrate the Bayesian Optimization concepts using an ordinary differential equation with two material properties to be estimated simultaneously. Next, we show how such an approach can simultaneously estimate five properties from a Hebb-Wagner test. Since the physics-based equations contain more information than just the macroscopic current/ voltage behavior at different material properties, one should be able to extract additional insights when physics-based equations are used to interpret experiments. We discuss such possibilities that extend the electroanalytical techniques beyond their analytical interpretation.

Table 1. An incomplete list of recent studies that estimate material properties from experiments using physics-based differential equations.

study	simultaneously estimated properties	experiments
Guo, Sethuraman and White (2004) [22]	gas-filled porosities of gas diffusion layer and catalyst layer, exchange current density, effective ionic conductivity, oxygen diffusivity in agglomerate particles	fuel cell polarization curves at difference electrode pressures
Santhanagopalan, Guo and White (2007) [23]	diffusivities and intercalation reaction rate constants	constant current operation of a full cell
Chadwick *et al*. (2016) [24]	diffusivity, rate constant, charge transfer coefficient, open circuit potential and nucleation overpotential	cyclic voltammetry

Brady, Gould & West (2017) [25]	diffusion coefficient, exchange current density, rate constant for the phase change reaction	current interrupt on half-cells
Ta, See & Gewirth (2018) [26]	reaction rate constants	cyclic and linear sweep voltammetry
Adams *et al*. (2019) [27]	enthalpies and rate constants for thermally activated reactions	differential scanning calorimetry on battery active material powder
Sethurajan *et al*. (2019) [28]	concentration dependence of diffusivity and transference number	constant current polarization of an electrolyte
Ta *et al*. (2019) [29]	reaction rate constants and diffusivity	linear sweep voltammetry
Horner *et al*. (2021) [30]	diffusivity	galvanostatic intermittent titration on a half-cell
Mayilvahanan *et al*. (2021) [31]	tortuosity	constant current operation of porous intercalation electrodes
Mistry *et al*. (2021) [32]	active area and tortuosity	constant current operation of porous intercalation electrodes
Fenton Jr. & Brushett (2022) [33]	open circuit voltage, diffusivities of redox species, charge transfer coefficient	voltammetry
Kuhn *et al*. (2022) [34]	diffusivities, exchange current densities, cation transference number, Bruggeman coefficients	galvanostatic intermittent titration on a full cell
Feng *et al*. (2023) [35]	enthalpies and rate constants for thermally activated reactions	differential scanning calorimetry on cells
Daniels *et al*. (2023) [36]	concentration dependence of exchange current density	constant current operation of full cells
this study	interfacial resistance, double layer capacitance, total conductivity, chemical diffusivity and Newman number	constant voltage behavior of dense active material pellets

BAYESIAN OPTIMIZATION

In recent years, a few studies[24,34] have employed Bayesian Optimization to estimate material properties (consistent with physics-based governing equations) of battery materials from experiments. Given that such an approach is still not widely used, we first illustrate essential concepts using a simple example. Consider current response governed by an ordinary differential equation

$$\frac{\mathrm{d}i}{\mathrm{d}t} = -i\left(\frac{1}{\tau} - \frac{1}{t}\right) \qquad [1]$$

subject to initial condition

$$i(t_0) = \alpha t_0 \qquad [2]$$

where t_0 is a small time. Two properties α (proportionality constant) and τ (time constant) appear in these equations. Exemplar measurements are shown in **Figure 1**(a), produced by solving Eqs. [1] and [2] for $\alpha = 1$ and $\tau = 2$[s] with a normally distributed noise of amplitude 0.05.

The traditional approach to estimating α and τ from such measurements relies on approximate solutions of the physics-based differential equations as shown in **Figure 1**(b) – (c). At very short times, it can be shown that

$$i(t) = \alpha t \qquad [3]$$

In the other extreme of long times,

$$\frac{\mathrm{d}i}{\mathrm{d}t} \approx -\frac{i}{\tau} \qquad [4]$$

i.e.,

$$\log i = -\frac{t}{\tau} + \text{constant} \qquad [5]$$

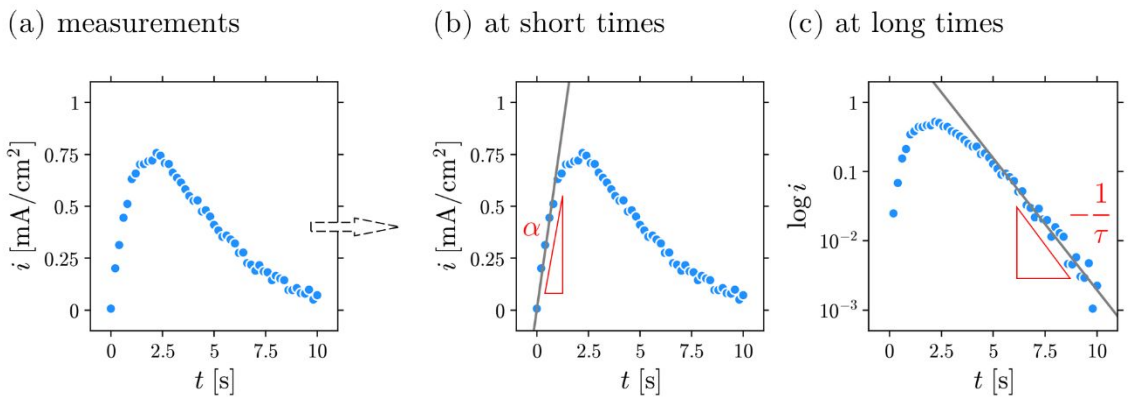

Figure 1. (a) Example measurement data for behavior describes by Eqs. [1] and [2]. Typical electroanalytical interpretation to estimate corresponding material properties, α and τ, are respectively shown in (b) and (c).

Accordingly, the slope of i versus t at short times, estimates α , and the slope of $\log i$ versus t at long times, estimates $-\frac{1}{\tau}$. The properties estimated in this fashion are mentioned in **Table 2**.

In contrast, the Bayesian Optimization-based approach solves physics (i.e., Eqs. [1] and [2]) for assumed property values. Every such solution is compared against the experimental measurements to compute the difference, Δ, expressed as

$$\Delta(\alpha,\tau) = \sqrt{\frac{1}{N_{\text{time points}}}\sum_{j=1}^{N_{\text{time points}}}\left(i_j^{\text{expt}} - i_j^{\text{theory}}(\alpha,\tau)\right)^2} \qquad [6]$$

and schematically shown as a shaded region in **Figure 2**(a). Initially, such exact calculations are carried out for N_{guesses} property values. The property values are randomly chosen in the search space. Given this set of $(\alpha_k,\tau_k,\Delta_k)$ values, a surrogate function is used to approximate the difference function over the entire search space. A typical choice for the surrogate function is a Gaussian Process. Mathematically,

$$\tilde{\Delta}(\alpha,\tau) = \text{Gaussian Process}\ (\alpha_k,\tau_k,\Delta_k) \qquad [7]$$

where $\tilde{\Delta}$ represents an approximate difference function. Any surrogate function should also provide a measure of uncertainty within the search space. The (α_k,τ_k) locations where the exact difference, Δ_k, is known have no uncertainty since they are precisely known. Other locations will exhibit varying levels of uncertainty depending on their proximity to these known locations. The Gaussian Process also provides such uncertainty information in the form of standard deviation, σ. Variations in $\tilde{\Delta}$ and σ over the search space for the initial N_{guesses} are plotted in **Figure 2**(b) and (c) respectively.

These two different pieces of information, $\tilde{\Delta}$ and σ, offer two different routes to identifying the next property combination where physics (Eqs. [1] and [2]) should be explicitly solved for:

i. locations with $\tilde{\Delta}$ smaller than the smallest of the exact differences, i.e., $\tilde{\Delta} < \min(\Delta_k)$, are promising;
ii. locations with high uncertainty are useful since corresponding regions have not been examined before.

An acquisition function, $\mathcal{A}$, combines these two information as per the expression:

$$\mathcal{A} = \left(\frac{\sigma}{\text{RMS}(\sigma)}\right)^{\xi}\left(\frac{\min(\Delta_k)}{\tilde{\Delta}}\right)^{(1-\xi)} \qquad [8]$$

where RMS ≡ root mean squared. Subsequently physics-based equations are explicitly solved for the property combination corresponding to $\max(\mathcal{A})$. Here $\xi \in [0,1]$ is a parameter that biases the decision for choosing the next property combination toward uncertainty information. The acquisition function map corresponding to **Figure 2**(b) and (c) is shown in **Figure 2**(d). **Figure 2**(e) identifies the new property combination explored based on **Figure 2**(d). Note that the uncertainty map (**Figure 2**(c)) shows the least uncertainty for the previously explored points (i.e., black dots in **Figure 2**(e)).

Such maps are for a visual understanding of the steps, and are not necessary for executing the Bayesian Optimization. Instead, one samples the surrogate function over a large number of points (say N_{samples}) to quantify $\mathcal{A}$ over the search space. It is advantageous to randomly generate these search points at every iteration, so every corner of the search space is sampled as the Bayesian Optimization progresses.

The property combination identified in this fashion and the corresponding explicit difference are appended to the $(\alpha_k,\tau_k,\Delta_k)$ set, and the same sequence of steps are repeated to improve the solution as shown in **Figure 2**. The

representative property values estimated in this fashion are enumerated in **Table 2**. The key advantage of the Bayesian Optimization is that the entire search space does not have to be explicitly examined to identify the solution. To understand how accurately the map of exact differences is inferred based on such a few property combinations arranged in an unstructured fashion, compare **Figure 3**(a) with (c). The surrogate difference map qualitatively matches the exact difference map. The region of minimum difference is also similar; however, the difference values are fairly different. This is an artefact of the use of Gaussian Process as a surrogate function. Since it is fundamentally a regression operation, it does not approach the exact difference values at the locations where the exact differences are available (regression approximately describes the underlying trend). This aspect is further clarified in **Figure 3**(d). Alternatively, any interpolation will recover the exact differences, e.g., **Figure 3**(e), and the corresponding difference map, **Figure 3**(b), better approximates the exact difference map in **Figure 3**(c). Despite the approximation, the estimated properties fairly describe the physics behavior underlying the measurements as shown in **Figure 3**(f).

The interpolated difference map can be further used to identify the property values close to the solution point that only slightly increase the difference value as shown in **Figure 3**(g). The error bars represent property combinations for which $\tilde{\Delta}_{\text{interpolation}} \leq 1.2 \times \min(\Delta_k)$. As is evident by the corresponding physics-based simulations in **Figure 3**(h), such a range of properties faithfully describe the measurements. Corresponding numerical values are identified in **Table 2**.

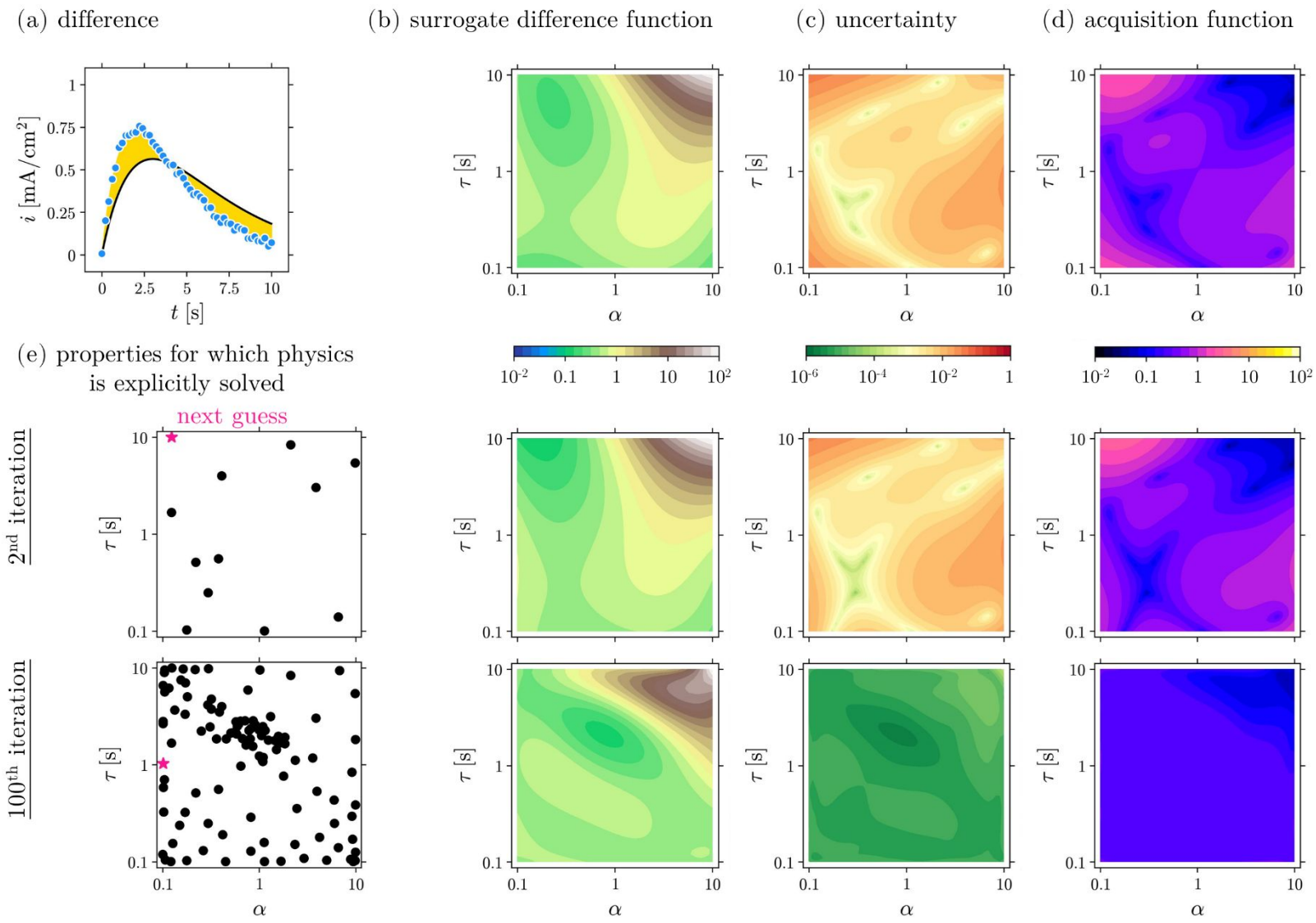

Figure 2. Illustrating different steps of the Bayesian Optimization algorithm. (a) For a given choice of properties, α and τ, one can solve Eqs. [1] and [2] to obtain a $i(t)$ behavior as shown by the continuous curve. The shaded region shows the difference between experimental measurements and such predictions. (b) Based on a few

initial guesses for α and τ (identified as black dots in (e)), one can compute such exact differences, Δ. Gaussian Process approximate such behavior, $\tilde{\Delta}$, over the entire search space as shown in (b). (c) The Gaussian Process also describes the corresponding uncertainty, σ. Larger values signify more uncertainty. Note that the smaller values coincide with black dots in (e). (d) An acquisition function, $\mathcal{A}$, combine both these information, $\tilde{\Delta}$, and σ, and ranks the points in the search space. The location with the highest $\mathcal{A}$ value is selected as the next property combination to explicitly solve the physics for. This sequence of operations is repeated to identify the property combinations with the smallest difference, i.e., most representative of the experimental measurements. Each row represents an iteration of this process.

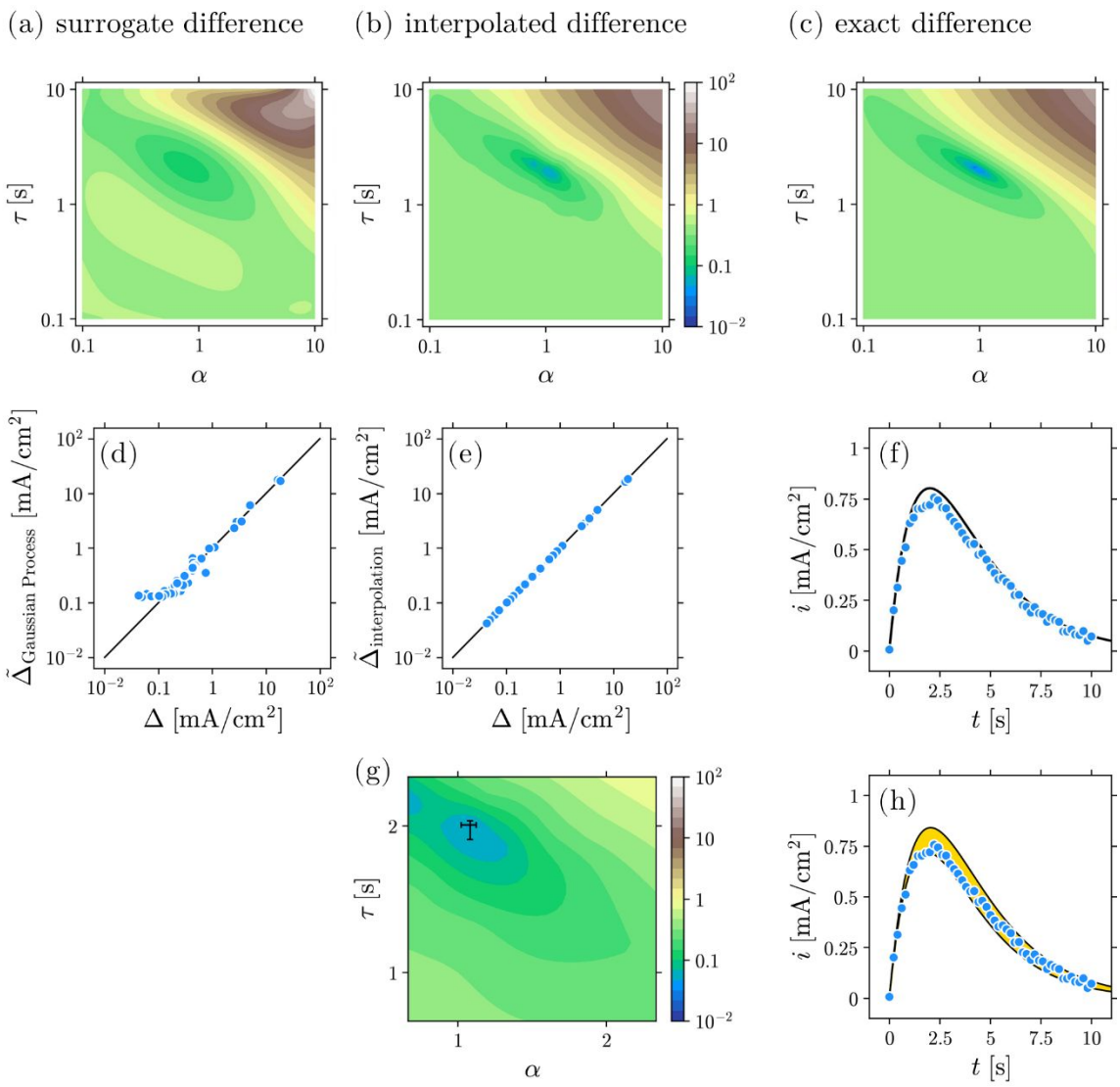

Figure 3. (a) Gaussian Process-based surrogate difference function is qualitatively identical to (b) interpolating using exact difference function computed at a few property combinations. Both of them capture the essential characteristics of (c) the exact difference over the entire search space. The difference between the surrogate (Gaussian Process-based) and interpolated difference function are clearer in (d) and (e): interpolation reproduces the exact values wherever available and interpolates for in-between points, while Gaussian Process is fundamentally a regression and does not necessarily recover the exact values. (f) Comparison of measurements and physics-based behavior corresponding to the estimated (i.e., smallest difference) property values. (g) Based on the interpolated difference function, the property combinations that are close to the minimum difference, here $\tilde{\Delta}_{\text{interpolation}} \leq 1.2 \times \min(\Delta_k)$, can be identified. Corresponding range of physical behaviors are shown in (h).

Since both the initial N_{guesses} property combinations and the N_{samples} points at every iteration are stochastically generated, re-applying the Bayesian Optimization algorithm to the same measurement will lead to a slightly different answer. Results from such five sets of calculations are also presented in **Table 2**.

The aforementioned steps for Bayesian Optimization are conceptually similar to other works[37,38]. The key difference is the specific choice of the acquisition function (Eq. [8]). The steps rely on three user-specified parameters: N_{guesses},ξ and N_{samples}.

- For a given choice of ξ and N_{samples}, similar $N_{\text{guesses}} + N_{\text{iterations}}$ are needed to reach comparable $\text{RMS}(\sigma)$ for a

given problem. RMS(σ) is an indicator for how accurately we know the behavior of the difference function over the property search space.

- As discussed earlier, ξ judiciously combines the two ways of identifying the next property combination for the explicit physics calculation. Depending on the specific problem, one of those could be more useful to identifying the solution and in turn a biased ξ, i.e., $\neq 0.5$, can be useful to more quickly identifying the solution. We did not have any such information about the problem and in turn we chose to use $\xi = 0.5$.
- A larger number of initial samples, N_{samples}, more thoroughly examines the search space at every iteration, however, very large N_{samples} slow down the execution as the surrogate function will be called upon to estimate more values. Note that library implementations like scikit-learn[39] do make this process efficient and one does not need to individually call the Gaussian Process to evaluate $\tilde{\Delta},\sigma$ for every sample point. Instead, $\tilde{\Delta},\sigma$ values are computed at all sample points by a single function call.

Table 2. Comparing estimated properties α and τ against exact properties used to generate experimental data shown in **Figure 1**(a). The range of property values indicated alongside the solution values correspond to the bars plotted in **Figure 3**(g).

	α	τ [s]
exact properties	1.00	2.00
traditional solution - **Figure 1**(b) and (c)	0.70	2.63
Figure 3 solution	1.06 (1.02 – 1.09)	2.00 (1.87 – 2.04)
repeat #1	0.94 (0.91 – 0.98)	1.91(1.85 – 1.99)
repeat #2	0.87(0.85 – 0.92)	2.07(2.02 – 2.13)
repeat #3	1.08(1.00 – 1.11)	1.98(1.89 – 2.04)
repeat #4	1.09(1.06 – 1.11)	1.81(1.77 – 1.87)
repeat #5	0.87(0.84 – 0.93)	2.05(2.01 – 2.14)

Another important aspect is the choice of the search space. As **Figure 2** and **Figure 3** show, we chose $\alpha \in [0.1,10]$ and $\tau \in [0.1,10]$. Two time constants are intrinsic to the measured signal in **Figure 1**(a): time between two consecutive measurements (here 0.1 [s]) and the total measurement time – 10 [s], and we chose them as the bounds on τ. Note that one could set narrower bounds by resorting to the Nyquist sampling criterion. Since α relates to the slope of the $i(t)$ data at early times, its bounds are set based on a visual examination of the measurements.

Thus, for a given choice of experimental measurements and physics governing equations, how quickly Bayesian Optimization finds meaningful properties relies on the choice of the acquisition function, $\mathcal{A}$, algorithmic parameters, N_{guesses},ξ, and N_{samples} (also referred to as hyperparameters) and the property search space.

ANALYZING HEBB-WAGNER MEASUREMENTS

To illustrate the usefulness of the aforementioned Machine Learning-based approach to simultaneously estimating multiple properties, consider the Hebb-Wagner test. It is an electroanalytical technique routinely employed to characterize mixed ionic and electronic conduction in solids[40–47]. Its traditional interpretation estimates two material properties by measuring initial and steady state currents during constant voltage (i.e., potentiostatic) holds. In the subsequent discussion, we show that instead of using initial and steady state current measurements, we can estimate multiple properties by analyzing the time evolution of current measurements.

Figure 4(a) schematically shows the experimental configuration for the Hebb-Wagner test. The corresponding current profiles are shown in **Figure 4**(b) and (c) (the experimental data is from our recent study[48]). As schematically shown in **Figure 4**(a), a dense pellet of $MgCr_2O_4$ – a mixed conductor – is sputter coated with Pt thin films. Given the high conductivity of Pt and its smaller thickness compared to the pellet (~100 [nm] versus ~1 [mm]), the measured current and voltage reflect signatures of bulk transport in the pellet and electron transfer at

Pt/pellet interfaces. The corresponding physics-based governing equations[48] are

$$\frac{\partial c}{\partial t} = \frac{\partial}{\partial x}\left(\mathcal{D}\left(1 - \frac{c}{c_{\max}}\right)\frac{\partial c}{\partial x} - t_+^{\Theta}\frac{i}{2F} - c v_{\Theta}\right) \quad [9]$$

$$\phi_0 - \phi_L = i\int_0^L \frac{1}{\sigma}\mathrm{d}x + \int_0^L t_+^{\Theta}\frac{3RT}{2F}\left(1 + \frac{\partial \log f_{M\Theta}}{\partial \log c}\right)\mathrm{d}\log c \quad [10]$$

subject to boundary conditions

$$-\mathcal{D}\left(1 - \frac{c}{c_{\max}}\right)\frac{\partial c}{\partial x} = -t_+^{\Theta}\frac{i}{2F} \quad [11]$$

$$i = i_R + i_C \quad [12]$$

$$i_R = \frac{1}{R_{\mathrm{i}}}\Delta\phi_{\mathrm{interface}} \quad [13]$$

$$i_C = C_{\mathrm{i}}\frac{\mathrm{d}(\Delta\phi_{\mathrm{interface}})}{\mathrm{d}t} \quad [14]$$

$$V_{\mathrm{app}} = \Delta\phi_{\mathrm{interface}} + (\phi_0 - \phi_L) \quad [15]$$

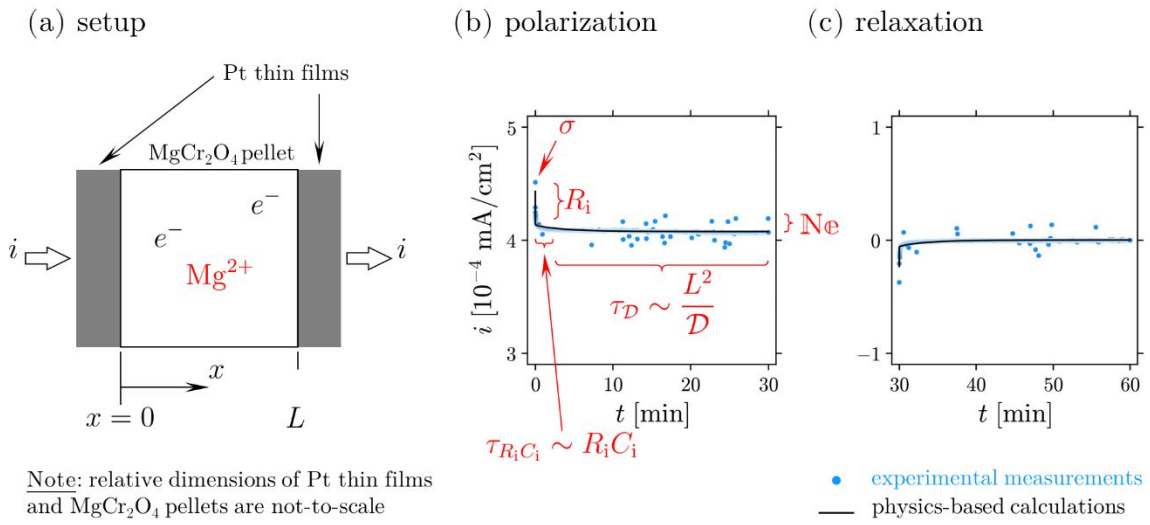

Figure 4. (a) Experimental setup for the Hebb-Wagner test. Corresponding (b) constant voltage, $V_{\mathrm{app}} = 1$ [V], polarization and (c) zero voltage relaxation behavior for a 0.98 [mm] thick, 98.1% dense $MgCr_2O_4$ pellet at 350 [°C]. Raw measurement data is borrowed from an earlier work by the authors[48]. The experimental data is collected every 0.5 [s] and most of the measurement point lie underneath the continuous theoretical trend in (b) and (c).

Note that R_{i} and C_{i} jointly describe the behavior of two identical interfaces. Thus, resistance of either interface is $R_{\mathrm{i}}/2$ and the corresponding capacitance is $2C_{\mathrm{i}}$. Also, concentration, c, describes the concentration of both the electrons and sites filled with Mg^{2+} (due to local charge neutrality) as $c = \frac{1}{2}c_{e^-} = c_{Mg^{\Theta 2+}}$. It can be shown that in the limit of small concentration perturbation such that the properties can be assumed constant for the duration of the experiments, these equations simplify to

$$\frac{\partial \tilde{c}}{\partial t} = \mathcal{D}\frac{\partial^2 \tilde{c}}{\partial x^2} \quad [16]$$

$$\phi_0 - \phi_L = \frac{1}{\sigma}\{iL + 2\mathbb{N}\mathbb{e}F\mathcal{D}(c_L - c_0)\} \quad [17]$$

subject to

$$-\mathcal{D}\frac{\partial \tilde{c}}{\partial x} = -\frac{i}{2F} \quad [18]$$

where c_{eq} is the uniform pellet concentration at the start of the test, while $\tilde{c}$ and $\mathbb{N}\mathbb{e}$ are defined as

$$\tilde{c} = \frac{(c - c_{\mathrm{eq}})}{t_+^{\Theta}\left(1 - \frac{c_{\mathrm{eq}}}{c_{\max}}\right)} \quad [19]$$

$$\mathbb{N}\mathbb{e} = \left(t_+^{\Theta}\right)^2\frac{3RT}{4F^2}\left(1 + \frac{\partial \log f_{M\Theta}}{\partial \log c}\right)\frac{\left(1 - \frac{c_{\mathrm{eq}}}{c_{\max}}\right)}{c_{\mathrm{eq}}\mathcal{D}} \quad [20]$$

Eqs. [12] – [15] are equally applicable. Thus, Eqs. [12] –[20] describe the experimental behavior. These expressions contain five measurable properties: R_{i},C_{i} (interfacial

properties) and σ,$\mathcal{D}$,$\mathbb{Ne}$ (bulk properties). In principle, each of these can be inferred from the experiments as long as they exhibit different detectable signatures as shown in **Figure 4**(b). While such a connection between physics governing equations and experimental measurements is intuitively clear, the analysis of the experimental measurements by solving Eqs. [12] –[20] is cumbersome as they do not exhibit an analytical solution and one has to computationally solve the governing equations for every choice of property values (this bottleneck has been one of the key reasons for popularity of electroanalytical techniques which can be interpreted by fitting analytical solutions to experimental measurements). Machine learning techniques like Bayesian Optimization make such an analysis computationally tractable.

Applying the same procedure as outlined earlier, these five properties are estimated. **Figure 4**(b) and (c) compare physics-based calculations using these estimated properties against measurements. Given simultaneous estimation of five properties, the corresponding difference map is five dimensional. **Figure 5**(a) and (d) illustrate its 2D cross-sections in the same spirit as **Figure 3**(b). Equivalently, **Figure 5**(b) and (c) sketch physics-based behavior corresponding to the property bounds identified in **Figure 5**(a) while **Figure 5**(e) and (f) refer to **Figure 5**(d). Note that we directly solve for R_i,$\tau_{R_iC_i}$,σ,$\tau_{\mathcal{D}}$ and $\mathbb{Ne}$ since it is more straightforward to specify search space for $\tau_{R_iC_i}$ and $\tau_{\mathcal{D}}$ instead of C_i and $\mathcal{D}$, respectively.

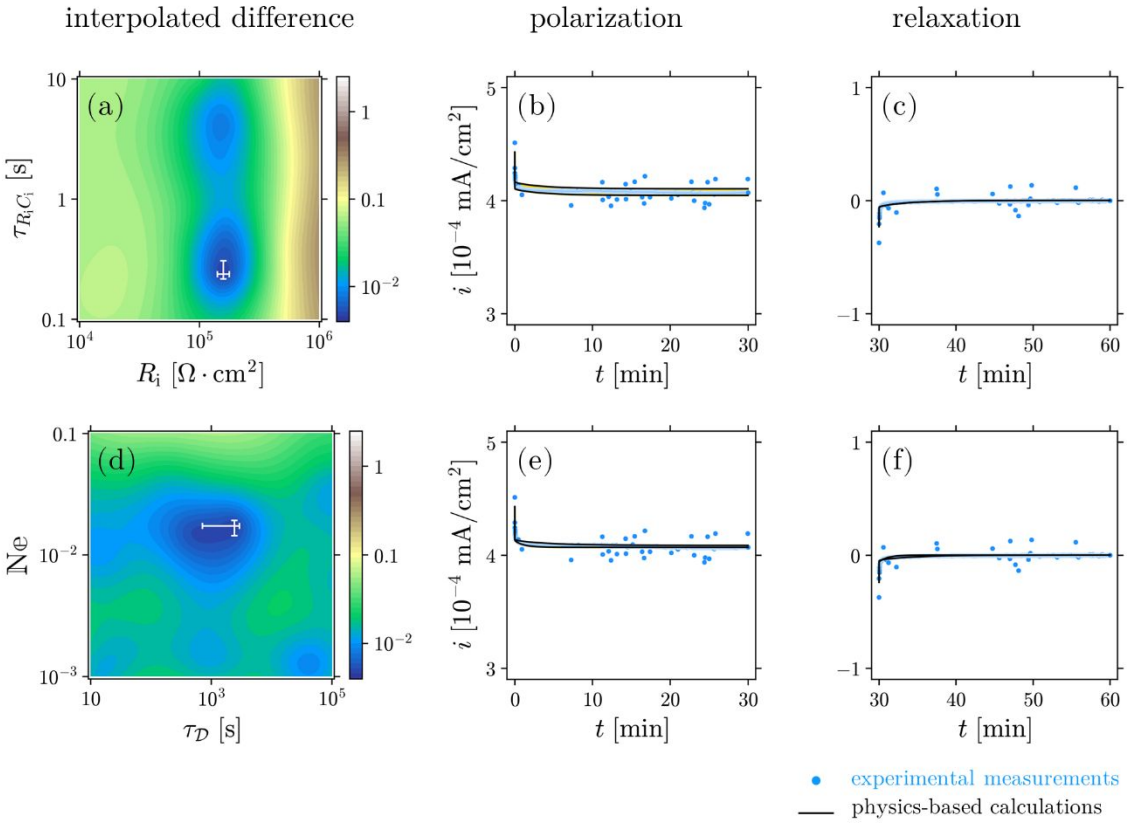

Figure 5. (a), (d) Interpolated difference maps corresponding to measurements reported in **Figure 4**(b) and (c). Each of the other three properties in (a) and (d) are kept fixed at their estimated values. (b), (c) and (e), (f) compare physics-based calculations against measurements, using the property bounds respectively identified in (a) and (d).

While the 2D difference maps in **Figure 3**(a), (b) and (g) clearly identify uniqueness of the estimated properties, **Figure 5**(a) and (d) only partially answer this. To further justify the uniqueness of the solution, **Figure 6** plots $\mathbb{Ne}$ versus $\tau_{\mathcal{D}}$ maps at different $(R_i,\tau_{R_iC_i})$ combinations and estimated σ. By comparing different maps in **Figure 6**, it is evident that the solution lies closer to **Figure 6**(i). As **Table 3** reveals, this is indeed the case. Note that as discussed before, the stochastic nature of Bayesian Optimization gives rise to slightly different properties with repeated runs (for a

given run of Bayesian Optimization, the uncertainty map prescribes if enough iterations have been carried out).

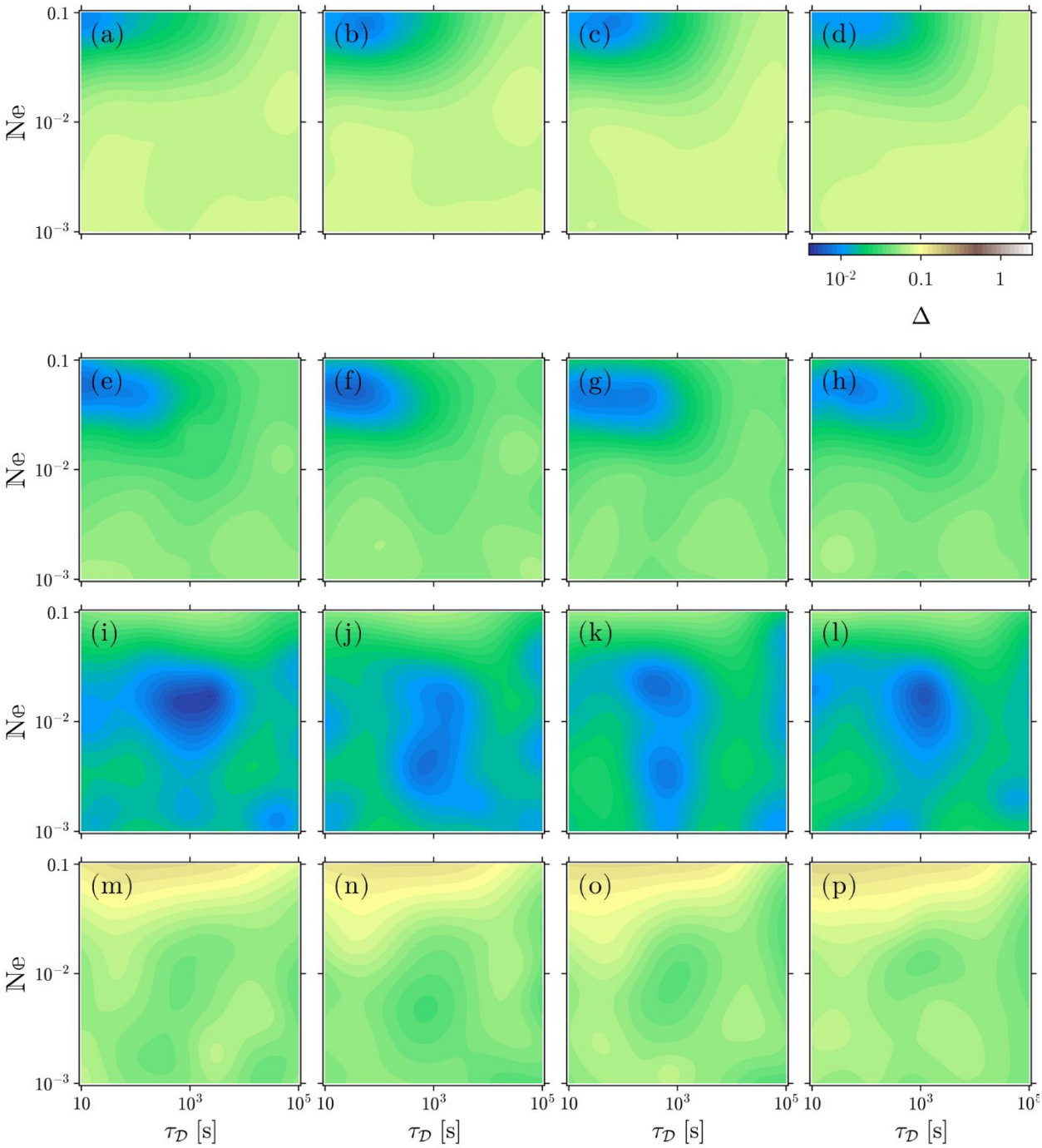

Figure 6. № versus $\tau_{\mathcal{D}}$ interpolated difference maps at different $(R_i,\tau_{R_iC_i})$ combinations and estimated σ value. Horizontal panels are at different $\tau_{R_iC_i} = 0.25, 0.63, 1.58$ and 3.98 [s], while the vertical panels are at different $R_i = 0.25, 0.63, 1.59$ and 3.98 $[10^5\ \Omega \cdot \mathrm{cm}^2]$. The colorbar is identical to **Figure 5**(a) and (d). The solution is closer to (i).

Table 3 reports multiple repeats to get a sense for such variance in estimated properties.

Apart from simultaneously solving for all the properties by analyzing the complete time series, another advantage of such an approach lies in its ability to report underlying fields since the corresponding physics-based equations are solved for each property combinations. **Figure 7** reports various concentration and potential fields corresponding to the solution reported in **Figure 4**(b) and (c).

Figure 7(a) and (d) sketch the evolution of interfacial potential drop, $\Delta\phi_{\text{interface}}$, respectively during polarization and subsequent relaxation. As is evident in **Figure 7**(a), the interfacial drop manifests within the first few seconds and stays invariant for the rest of the polarization. Equivalently, during relaxation, it diminishes within a similar timeframe. Recall that $\Delta\phi_{\text{interface}}$ describes the behavior of both the interfaces, i.e., either of the interface experiences half the potential drop. Here $\Delta\phi_{\text{interface}}/V_{\text{app}}$ is reported to express the contribution of $\Delta\phi_{\text{interface}}$ to the overall response.

Figure 7(b), (c), (e) and (f) present bulk fields across the pellet thickness. Since during polarization, electrons enter from $x = L$ and leave from $x = 0$, the evolution of the concentration profiles in **Figure 7**(b) is intuitive. Given local charge neutrality, the flux of filled Mg^{2+} sites ensures their equivalent distribution. During relaxation, the concentration relaxes as shown in **Figure 7**(e). Note that the slopes of the concentration profiles differ across **Figure 7**(b) and (e) since as per Eq. [18], the slopes directly relate to the current density, i. The different behaviors of i in **Figure 4**(b) and (c) accounts for these features in concentration profiles. Given identical electronic charges enter and leave from the two interfaces, the total pellet concentration does not change, i.e., $\int_0^L \tilde{c}\mathrm{d}x = 0$.

Table 3. Comparing variability in properties estimated from the same experimental measurements reported in **Figure 4**(b) and (c) as symbols. Such a variation is due to the stochastic nature of the Bayesian Optimization algorithm.

	interfacial properties		bulk properties		
	$R_{\text{i}}\,[10^5\,\Omega\cdot\text{cm}^2]$	$\tau_{R_{\text{i}}C_{\text{i}}}$ [s]	$\sigma\,[10^{-8}\,\text{S/cm}]$	$\mathcal{D}\,[10^{-10}\,\text{cm}^2/\text{s}]$	$\mathbb{N}\mathbb{e}\,[10^{-2}]$
Figure 4 solution	1.59 (1.42 — 1.78)	0.24 (0.22 — 0.31)	4.34 (4.33 — 4.35)	3.94 (3.26 — 13.43)	1.73 (1.43 — 1.91)
repeat #1	2.58 (2.37 — 2.73)	0.13 (0.12 — 0.14)	4.51 (4.50 — 4.51)	2.83 (2.48 — 3.31)	1.00 (0.93 — 1.09)
repeat #2	1.65 (1.50 — 1.80)	0.65 (0.61 — 0.84)	4.33 (4.32 — 4.34)	4.83 (3.91 — 6.03)	1.19 (1.10 — 1.34)
repeat #3	1.58 (1.45 — 1.73)	0.71 (0.65 — 0.80)	4.33 (4.32 — 4.33)	3.96 (3.20 — 4.74)	1.64 (1.52 — 1.85)
repeat #4	2.51 (2.35 — 2.68)	0.18 (0.17 — 0.20)	4.48 (4.47 — 4.48)	1.17 (1.01 — 1.33)	0.76 (0.71 — 0.82)
Repeat #5	2.34 (2.12 — 2.56)	0.80 (0.72 — 0.89)	4.47 (4.46 — 4.50)	3.47 (2.96 — 4.79)	1.14 (1.04 — 1.27)

Combining Eqs. [10], [15] and [17], it can be shown that the applied voltage drop, V_{app}, is composed of three distinct contributions: interfacial drop, $\Delta\phi_{\text{interface}}$, ohmic drop, and concentration overpotential. The latter two relate to the bulk fields and equivalently their spatial dependence can be mathematically expressed as

$$\Delta\phi_{\text{ohmic}}(x) = i\frac{x}{\sigma} \qquad [21]$$

$$\Delta\phi_{\text{conc}}(x) = \frac{1}{\sigma}2\mathbb{N}\mathbb{e}F\mathcal{D}(c_L - c(x)) \qquad [22]$$

The ohmic drop is straightforward to imagine. Hence, **Figure 7**(c) and (f) sketch the concentration overpotential. It is important to note that the concentration overpotential is about 10% of the applied voltage when the polarization approaches the steady state. The distribution of the different potential drops varies across different materials or testing of the same material at different pellet thicknesses or measurement temperatures.

DISCUSSION

Figure 8 presents the conceptual differences among the traditional electroanalytical tests, physics-based theory and herein highlighted emerging approach based on machine learning. While physics-based theory predicts fields and macroscopic behavior corresponding to prescribed properties, the electroanalytical techniques pose an inverse problem of estimating properties from macroscopic measurements. The emerging approach of using machine learning techniques, e.g., Bayesian Optimization, to interpret electroanalytical tests in a physics-consistent fashion has two obvious advantages:

- Since the full experimental timeseries is analyzed, multiple properties are estimated simultaneously. For example, traditionally, the Hebb-Wagner test[40,41,49] is

only analyzed for its initial and steady state currents, which respectively characterize σ and $\mathbb{Ne}$ (or the transference number if the material exhibits conventional mixed conduction). Instead, the aforementioned analysis simultaneously characterizes R_i,C_i, σ,$\mathcal{D}$ and $\mathbb{Ne}$, from the same data (traditionally, it would have required additional electroanalytical tests to characterize R_i,C_i and $\mathcal{D}$[40,50–53]). Such an estimation of multiple properties from a single experiment does not overfit he physics as long as each of these properties exhibit distinct signatures, e.g., as identified in **Figure 4**(b).

- In addition to the estimated properties, various concentration and potential fields are computationally available for the duration of the experiments. Such information is not available from direct analytical interpretation of the electroanalytical tests.

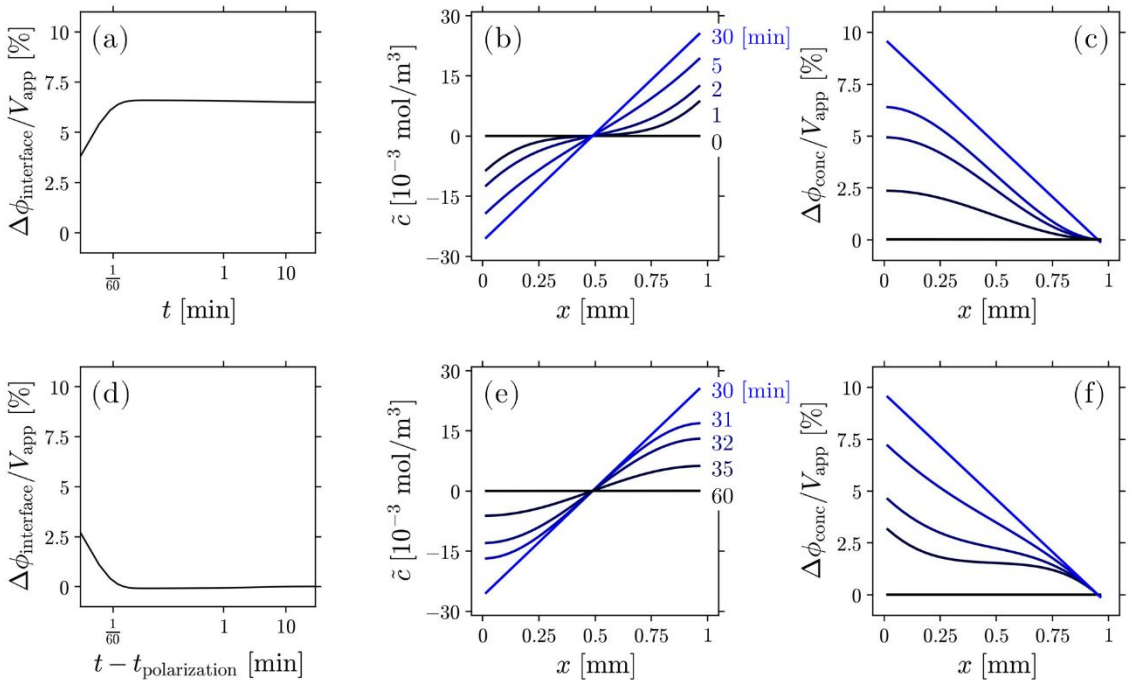

Figure 7. Internal fields corresponding to physics-based solution reported in **Figure 4**(b) and (c). (a), (b) and (c) refer to polarization, while (d), (e) and (f) relate to relaxation. $\tilde{c}$ is defined in Eq. [19]. $\Delta\phi_{\text{conc}}$ is defined in Eq. [22].

The first advantage reduces the experimental efforts and in turn expands the scope of robotic experiments for material screening. The second advantage provides previously inaccessible information that can be compared against imaging experiments[54,55] to identify missing physics. For example, the electrolyte literature assumed that the solvent does not move when an electrolyte is polarized since it is a charge neutral species. Recent X-ray Photon Correlation Spectroscopy experiments revealed a distinct presence of solvent motion[56] which in turn has extended the understanding of electrolyte transport to incorporate an overlooked physics of solvent motion in response to concentration gradients and currents[17].

Often analytical solutions not only solve physics under a select few operating conditions, but physics is also simplified. Such simplifications often lead to erroneous interpretation of the measurements, e.g., the Hebb-Wagner test is known to suffer many limitations[57] if interpreted casually. For another example, consider the galvanostatic intermittent titration test – a widely used test to measure diffusion in electrochemically intercalating hosts. Its traditional interpretation assumes[58–60] that the particles are spherical, their entire surface area is available for intercalation, intercalation is limited by ion diffusion and follows a solid solution mechanism. Depending on the context each of these assumptions can be violated and the standard analysis becomes invalid. Instead, the emerging approach in **Figure 8** would retain its validity and account for such additional material complexities as long as the underlying physics has been meticulously verified.

In many such instances, a traditional analytical interpretation may not even identify that the material

exhibits unexpected behavior. For example, the Hebb-Wagner measurements shown in **Figure 4**(b) and (c) do not exhibit the conventional mixed ionic electronic conduction behavior[61–64]. However, a traditional interpretation using initial and steady state currents would not have identified the breakdown of the conventional mixed conduction theory. Only when the complete current versus time data were interpreted using the conventional mixed conduction theory, the atypical behavior became apparent[48].

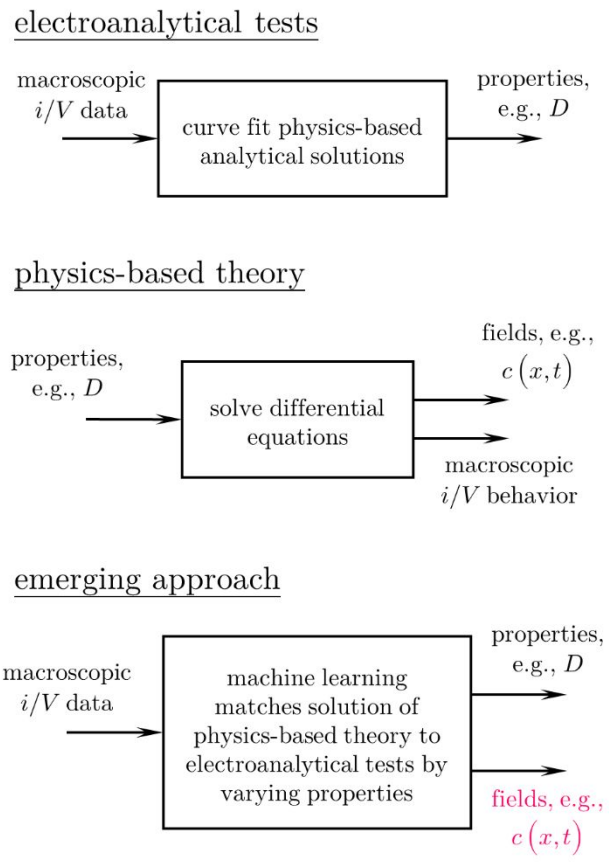

Figure 8. Conceptual differences across traditional electroanalytical tests, physics-based theory and the emerging machine learning-based approach (discussed herein) lie in the information they use and/or provide.

A thought-provoking question is how many different properties can be identified? As long as each of the properties exhibit differentiable signatures, it is possible to estimate them simultaneously. A related concern with an ML-based interpretation of electroanalytical techniques is uniqueness of the estimated properties. In addition to each of the estimated properties exhibiting differentiable signatures, one should justify the estimated property values by examining difference landscapes (e.g., **Figure 5**(a), (d) and **Figure 6**), comparing changes in physics-predicted behavior with small changes in the estimated properties against experimental data (i.e., **Figure 5**(b), (c), (e) and (f)) and quantifying repeatability of the solution (for example, **Table 3**). Such sense checks should be employed to justify that the ML-based interpretation of the experimental data is meaningful.

Another concern is the cost of analysis. Since the physics equations are numerically solved, such an implementation is computationally expensive. Of various machine learning algorithms, Bayesian Optimization is designed such that physics is explicitly solved at only the most promising property combinations. Thus, the choice of the specific machine learning algorithm helps manage computational expenses. There are other equivalent machine learning techniques that explicitly solve physics at a few selected property combinations to estimate properties from experimental measurements, e.g.,[65], and can be used to extend the electroanalytical measurements as advocated here. Alternatively, the same problem could have been cast as a deep neural network that is trained on a large combination of explicit physics solutions. However, it would require many more explicit solutions. Interestingly, deep neural networks that are trained using physics equations as the loss functions[66,67] could provide another efficient approach. Note that one can further reduce the computational time by solving physics in a faster programming language like Fortran or C while a python or a MATLAB script executes the machine learning aspects. Often, the scripting languages offer special libraries to dynamically link them to Fortran, C or C++, e.g., F2PY[68]. We leveraged such functionality to analyze the Hebb-Wagner data discussed in **Figure 4**.

Given the conceptual and computational overheads associated with the proposed approach, one should adopt it judiciously. If the physics equations can be solved analytically for the entire experiment, one should use it for regression over the experimental data, for example, under certain conditions, the Hebb-Wagner tests do exhibit analytical solutions[69,70]. However, if the analytical solutions are only available for limited experimental data, e.g., short time and/or long time, or if the analytical solution does not exist, one should prefer the emerging approach advocated here (compare across different rows in **Table 2**).

CONCLUSIONS

While electroanalytical techniques have been historically used to measure properties of materials relevant to electrochemical systems, ongoing and future efforts in understanding material behavior require (i) screening a material for desired properties and (ii) probing more complex material behaviors. Both of these applications pose challenges for traditional electroanalytical techniques (given their use of analytical solutions for interpreting properties,

they either require prohibitively high experimental efforts for materials screening and/ or fail to capture complex material behavior).

An emerging approach is to use the physics-based governing equations to interpret the electroanalytical tests. Machine learning techniques like Bayesian Optimization ensure manageable computational costs for such analyses. Such a synergistic combination of electroanalytical experiments, physics-based theory and machine learning techniques simultaneously estimates multiple properties from a single experiment as well as offer information about the underlying fields like concentration and potential. Thus, qualitatively and quantitatively more information is inferred from the electroanalytical experiments. The field information is uniquely valuable to independently assess our physics-based understanding of the material response against imaging measurements. Additionally, analysis of the full electroanalytical tests offers a route to interpreting more complex material behavior in contrast to analyzing limiting instances, e.g., short time/ high frequency response.

Thus, machine learning assisted physics consistent interpretation of the electroanalytical tests is a promising route to understanding electrochemical behavior of materials.

ACKNOWLEDGMENTS This work was supported by the Joint Center for Energy Storage Research (JCESR), an Energy Innovation Hub funded by the U.S. Department of Energy (DOE), Office of Science, Basic Energy Sciences (BES). The submitted manuscript has been created by UChicago Argonne, LLC, Operator of Argonne National Laboratory ("Argonne"). Argonne, a U.S. Department of Energy Office of Science laboratory, is operated under Contract No. DE-AC02–06CH11357. The U.S. Government retains for itself, and others acting on its behalf, a paid-up nonexclusive, irrevocable worldwide license in said article to reproduce, prepare derivative works, distribute copies to the public, and perform publicly and display publicly, by or on behalf of the Government. The Department of Energy will provide public access to these results of federally sponsored research in accordance with the DOE Public Access Plan http://energy.gov/downloads/doe-public-access-plan.

AM appreciates discussions with Rajeev Assary, Pallab Barai, Hieu Doan and Akash Jain.

REFERENCES

(1) Newman, J.; Balsara, N. P. *Electrochemical Systems, 4e*; John Wiley & Sons, 2021.

(2) Bard, A. J.; Faulkner, L. R. *Electrochemical Methods Fundamentals of Electrochemistry*; 2001.

(3) Dave, A.; Mitchell, J.; Kandasamy, K.; Wang, H.; Burke, S.; Paria, B.; Póczos, B.; Whitacre, J.; Viswanathan, V. Autonomous Discovery of Battery Electrolytes with Robotic Experimentation and Machine Learning. *Cell Reports Physical Science* **2020**, *1* (12), 100264. https://doi.org/10.1016/j.xcrp.2020.100264.

(4) Dave, A.; Mitchell, J.; Burke, S.; Lin, H.; Whitacre, J.; Viswanathan, V. Autonomous Optimization of Non-Aqueous Li-Ion Battery Electrolytes via Robotic Experimentation and Machine Learning Coupling. *Nature Communications* **2022**, *13* (1), 5454. https://doi.org/10.1038/s41467-022-32938-1.

(5) Bruce, P. G.; Vincent, C. A. Steady State Current Flow in Solid Binary Electrolyte Cells. *Journal of Electroanalytical Chemistry* **1987**, *225* (1–2), 1–17. https://doi.org/10.1016/0022-0728(87)80001-3.

(6) Newman, J.; Chapman, T. W. Restricted Diffusion in Binary Solutions. *AIChE Journal* **1973**, *19* (2), 343–348. https://doi.org/10.1002/aic.690190220.

(7) Ma, Y.; Doyle, M.; Fuller, Thomas. F.; Doeff, M. M.; De Jonghe, L. C.; Newman, J. The Measurement of a Complete Set of Transport Properties for a Concentrated Solid Polymer Electrolyte Solution. *Journal of The Electrochemical Society* **1995**, *142* (6), 1859–1868. https://doi.org/10.1149/1.2044206.

(8) Pesko, D. M.; Timachova, K.; Bhattacharya, R.; Smith, M. C.; Villaluenga, I.; Newman, J.; Balsara, N. P. Negative Transference Numbers in Poly(Ethylene Oxide)-Based Electrolytes. *Journal of The Electrochemical Society* **2017**, *164* (11), E3569–E3575. https://doi.org/10.1149/2.0581711jes.

(9) Landesfeind, J.; Gasteiger, H. A. Temperature and Concentration Dependence of the Ionic Transport Properties of Lithium-Ion Battery Electrolytes. *Journal of The Electrochemical Society* **2019**, *166* (14), A3079–A3097. https://doi.org/10.1149/2.0571912jes.

(10) Landesfeind, J.; Hosaka, T.; Graf, M.; Kubota, K.; Komaba, S.; Gasteiger, H. A. Comparison of Ionic Transport Properties of Non-Aqueous Lithium and Sodium Hexafluorophosphate Electrolytes. *Journal of The Electrochemical Society* **2021**, *168* (4), 40538. https://doi.org/10.1149/1945-7111/abf8d9.

(11) Hou, T.; Monroe, C. W. Composition-Dependent Thermodynamic and Mass-Transport Characterization of Lithium Hexafluorophosphate in Propylene Carbonate. *Electrochimica Acta* **2020**, *332*, 135085. https://doi.org/10.1016/j.electacta.2019.135085.

(12) Wang, A. A.; Hou, T.; Karanjavala, M.; Monroe, C. W. Shifting-Reference Concentration Cells to Refine Composition-Dependent Transport Characterization of Binary Lithium-Ion Electrolytes. *Electrochimica Acta* **2020**, *358*, 136688. https://doi.org/10.1016/j.electacta.2020.136688.

(13) Valøen, L. O.; Reimers, J. N. Transport Properties of LiPF[Sub 6]-Based Li-Ion Battery Electrolytes. *Journal of The Electrochemical Society* **2005**, *152* (5), A882–A891. https://doi.org/10.1149/1.1872737.

(14) Lundgren, H.; Behm, M.; Lindbergh, G. Electrochemical Characterization and Temperature Dependency of Mass-Transport Properties of LiPF 6 in EC:DEC. *Journal of The Electrochemical Society* **2015**, *162* (3), A413–A420. https://doi.org/10.1149/2.0641503jes.

(15) Nyman, A.; Behm, M.; Lindbergh, G. Electrochemical Characterisation and Modelling of the Mass Transport Phenomena in LiPF6-EC-EMC Electrolyte. *Electrochimica Acta* **2008**, *53* (22), 6356–6365. https://doi.org/10.1016/j.electacta.2008.04.023.

(16) Balsara, N. P.; Newman, J. Relationship between Steady-State Current in Symmetric Cells and Transference Number of Electrolytes Comprising Univalent and Multivalent Ions. *Journal of The Electrochemical Society* **2015**, *162* (14), A2720–A2722. https://doi.org/10.1149/2.0651514jes.

(17) Mistry, A.; Grundy, L. S.; Halat, D. M.; Newman, J.; Balsara, N. P.; Srinivasan, V. Effect of Solvent Motion on Ion Transport in Electrolytes. *Journal of The Electrochemical Society* **2022**, *169* (4), 040524. https://doi.org/10.1149/1945-7111/ac6329.

(18) Mistry, A.; Franco, A. A.; Cooper, S. J.; Roberts, S. A.; Viswanathan, V. How Machine Learning Will Revolutionize Electrochemical Sciences. *ACS Energy Letters* **2021**, 1422–1431. https://doi.org/10.1021/acsenergylett.1c00194.

(19) Agarwal, G.; Doan, H. A.; Robertson, L. A.; Zhang, L.; Assary, R. S. Discovery of Energy Storage Molecular Materials Using Quantum Chemistry-Guided Multiobjective Bayesian Optimization. *Chem. Mater.* **2021**, *33* (20), 8133–8144. https://doi.org/10.1021/acs.chemmater.1c02040.

(20) Wang, Y.; Xie, T.; France-Lanord, A.; Berkley, A.; Johnson, J. A.; Shao-Horn, Y.; Grossman, J. C. Toward Designing Highly Conductive Polymer Electrolytes by Machine Learning Assisted Coarse-Grained Molecular Dynamics. *Chemistry of Materials* **2020**, *32* (10), 4144–4151. https://doi.org/10.1021/acs.chemmater.9b04830.

(21) Vandermause, J.; Torrisi, S. B.; Batzner, S.; Xie, Y.; Sun, L.; Kolpak, A. M.; Kozinsky, B. On-the-Fly Active Learning of Interpretable Bayesian Force Fields for Atomistic Rare Events. *npj Computational Materials* **2020**, *6* (1), 20. https://doi.org/10.1038/s41524-020-0283-z.

(22) Guo, Q.; Sethuraman, V. A.; White, R. E. Parameter Estimates for a PEMFC Cathode. *Journal of The Electrochemical Society* **2004**, *151* (7), A983. https://doi.org/10.1149/1.1747850.

(23) Santhanagopalan, S.; Guo, Q.; White, R. E. Parameter Estimation and Model Discrimination for a Lithium-Ion Cell. *Journal of The Electrochemical Society* **2007**, *154* (3), A198. https://doi.org/10.1149/1.2422896.

(24) Chadwick, A. F.; Vardar, G.; DeWitt, S.; Sleightholme, A. E. S.; Monroe, C. W.; Siegel, D. J.; Thornton, K. Computational Model of Magnesium Deposition and Dissolution for Property Determination via Cyclic Voltammetry. *Journal of The Electrochemical Society* **2016**, *163* (9), A1813–A1821. https://doi.org/10.1149/2.0031609jes.

(25) Brady, N. W.; Gould, C. A.; West, A. C. Quantitative Parameter Estimation, Model Selection, and Variable Selection in Battery Science. *Journal of The Electrochemical Society* **2020**, *167* (1), 013501. https://doi.org/10.1149/2.0012001jes.

(26) Ta, K.; See, K. A.; Gewirth, A. A. Elucidating Zn and Mg Electrodeposition Mechanisms in Nonaqueous Electrolytes for Next-Generation Metal Batteries. *Journal of Physical Chemistry C* **2018**, *122* (25), 13790–13796. https://doi.org/10.1021/acs.jpcc.8b00835.

(27) Adams, R. A.; Mistry, A. N.; Mukherjee, P. P.; Pol, V. G. Materials by Design: Tailored Morphology and Structures of Carbon Anodes for Enhanced Battery Safety. *ACS Applied Materials and Interfaces* **2019**, *11* (14), 13334–13342. https://doi.org/10.1021/acsami.9b02921.

(28) Sethurajan, A. K.; Foster, J. M.; Richardson, G.; Krachkovskiy, S. A.; Bazak, J. D.; Goward, G. R.; Protas, B. Incorporating Dendrite Growth into Continuum Models of Electrolytes: Insights from NMR Measurements and Inverse Modeling. *Journal of The Electrochemical Society* **2019**, *166* (8), A1591–A1602. https://doi.org/10.1149/2.0921908jes.

(29) Ta, K.; Zhang, R.; Shin, M.; Rooney, R. T.; Neumann, E. K.; Gewirth, A. A. Understanding Ca Electrodeposition and Speciation Processes in Nonaqueous Electrolytes for Next-Generation Ca-Ion Batteries. *ACS Applied Materials and Interfaces* **2019**, *11* (24), 21536–21542. https://doi.org/10.1021/acsami.9b04926.

(30) Horner, J. S.; Whang, G.; Ashby, D. S.; Kolesnichenko, I. V.; Lambert, T. N.; Dunn, B. S.; Talin, A. A.; Roberts, S. A. Electrochemical Modeling of GITT Measurements for Improved Solid-State Diffusion Coefficient Evaluation. *ACS Applied Energy Materials* **2021**. https://doi.org/10.1021/acsaem.1c02218.

(31) Mayilvahanan, K. S.; Hui, Z.; Hu, K.; Kuang, J.; McCarthy, A. H.; Bernard, J.; Wang, L.; Takeuchi, K. J.; Marschilok, A. C.; Takeuchi, E. S.; West, A. C. Quantifying Uncertainty in Tortuosity Estimates for Porous Electrodes. *Journal of The Electrochemical Society* **2021**, *168* (7), 070537. https://doi.org/10.1149/1945-7111/ac1316.

(32) Mistry, A.; Trask, S.; Dunlop, A.; Jeka, G.; Polzin, B.; Mukherjee, P. P.; Srinivasan, V. Quantifying Negative Effects of Carbon-Binder Networks from Electrochemical Performance of Porous Li-Ion Electrodes. *Journal of The Electrochemical Society* **2021**, *168* (7), 70536. https://doi.org/10.1149/1945-7111/ac1033.

(33) Fenton Jr., A. M.; Brushett, F. R. Using Voltammetry Augmented with Physics-Based Modeling and Bayesian Hypothesis Testing to Identify Analytes in Electrolyte Solutions. *Journal of Electroanalytical Chemistry* **2022**, *904*, 115751. https://doi.org/10.1016/j.jelechem.2021.115751.

(34) Kuhn, Y.; Wolf, H.; Latz, A.; Horstmann, B. Bayesian Parameterization of Continuum Battery Models from Featurized Electrochemical Measurements Considering Noise**. *Batteries & Supercaps* **2023**, *6* (1), e202200374. https://doi.org/10.1002/batt.202200374.

(35) Feng, Y.-F.; Wang, C.; Shen, J.-N.; He, Y.-J. Kinetic Resolution of Thermal Runaway for Lithium-Ion Batteries: A Gaussian Surrogate-Assisted Separate Optimization Approach. *Chemical Engineering Science* **2023**, *277*, 118875. https://doi.org/10.1016/j.ces.2023.118875.

(36) Daniels, L.; Sahu, S.; Sanders, K. J.; Goward, G. R.; Foster, J. M.; Protas, B. Learning Optimal Forms of Constitutive Relations Characterizing Ion Intercalation from Data in Mathematical Models of Lithium-Ion Batteries. *arXiv preprint arXiv:2305.03185* **2023**.

(37) Frazier, P. I. A Tutorial on Bayesian Optimization. *arXiv preprint arXiv:1807.02811* **2018**.

(38) B. Shahriari; K. Swersky; Z. Wang; R. P. Adams; N. de Freitas. Taking the Human Out of the Loop: A Review of Bayesian Optimization. *Proceedings of the IEEE* **2016**, *104* (1), 148–175. https://doi.org/10.1109/JPROC.2015.2494218.

(39) Pedregosa, F.; Varoquaux, G.; Gramfort, A.; Michel, V.; Thirion, B.; Grisel, O.; Blondel, M.; Prettenhofer, P.; Weiss, R.; Dubourg, V. Scikit-Learn: Machine Learning in Python. *the Journal of machine Learning research* **2011**, *12*, 2825–2830.

(40) Wang, M. J.; Wolfenstine, J. B.; Sakamoto, J. Mixed Electronic and Ionic Conduction Properties of Lithium Lanthanum Titanate. *Advanced Functional Materials* **2020**, *30* (10), 1909140. https://doi.org/10.1002/adfm.201909140.

(41) Riess, I. Four Point Hebb-Wagner Polarization Method for Determining the Electronic Conductivity in Mixed Ionic-Electronic Conductors. *Solid State Ionics* **1992**, *51* (3), 219–229. https://doi.org/10.1016/0167-2738(92)90204-3.

(42) Maier, J. Mass Transport in the Presence of Internal Defect Reactions—Concept of Conservative Ensembles: II, Evaluation of Electrochemical Transport Measurements. *Journal of the American Ceramic Society* **1993**, *76* (5), 1218–1222. https://doi.org/10.1111/j.1151-2916.1993.tb03744.x.

(43) Preis, W. Non-Cottrell Behaviour of Potentiostatic Processes in Mixed Conductors with Comparable Ionic and Electronic Conductivities. *Berichte der Bunsengesellschaft für physikalische Chemie* **1997**, *101* (1), 50–58. https://doi.org/10.1002/bbpc.19971010106.

(44) Preis, W.; Sitte, W. Theory of Galvanostatic Processes in Mixed Conductors with Arbitrary Electronic Transport Numbers. *J. Chem. Soc., Faraday Trans.* **1996**, *92* (7), 1197–1203. https://doi.org/10.1039/FT9969201197.

(45) Preis, W.; Sitte, W. Polarization Studies on Mixed Conductors with Comparable Ionic and Electronic Conductivities Employed in Asymmetric Electrochemical Cells. *Solid State Ionics* **1996**, *86–88*, 779–784. https://doi.org/10.1016/0167-2738(96)00172-5.

(46) Preis, W.; Sitte, W. Electrochemical Cell for Composition-Dependent Electronic Conductivity and Chemical Diffusion Coefficient Measurements Applied to Mixed-Conductivity Intercalation Compounds. *J. Chem. Soc., Faraday Trans.* **1995**, *91* (14), 2127–2132. https://doi.org/10.1039/FT9959102127.

(47) Preis, W.; Sitte, W. Electrochemical Cell for Composition Dependent Measurements of Electronic and Ionic Conductivities of Mixed Conductors and Application to Silver Telluride. *Solid State Ionics* **1995**, *76* (1), 5–14. https://doi.org/10.1016/0167-2738(94)00246-O.

(48) Johnson, I. D.; Mistry, A. N.; Yin, L.; Murphy, M.; Wolfman, M.; Fister, T. T.; Lapidus, S. H.; Cabana, J.; Srinivasan, V.; Ingram, B. J. Unconventional Charge Transport in MgCr2O4 and Implications for Battery Intercalation Hosts. *J. Am. Chem. Soc.* **2022**, *144* (31), 14121–14131. https://doi.org/10.1021/jacs.2c03491.

(49) Maier, J. Electrochemical Investigation Methods of Ionic Transport Properties in Solids. In *Solid State Phenomena*; Trans Tech Publ, 1994; Vol. 39, pp 35–60.

(50) Amin, R.; Chiang, Y.-M. Characterization of Electronic and Ionic Transport in Li 1-x Ni 0.33 Mn 0.33 Co 0.33 O 2 (NMC 333) and Li 1- x Ni 0.50 Mn 0.20 Co 0.30 O 2 (NMC 523) as a Function of Li Content. *Journal of The Electrochemical Society* **2016**, *163* (8), A1512–A1517. https://doi.org/10.1149/2.0131608jes.

(51) Amin, R.; Lin, C.; Maier, J. Aluminium-Doped LiFePO4 Single Crystals: Part II. Ionic Conductivity, Diffusivity and Defect Model. *Physical Chemistry Chemical Physics* **2008**, *10* (24), 3524–3529. https://doi.org/10.1039/b801795f.

(52) Amin, R.; Balaya, P.; Maier, J. Anisotropy of Electronic and Ionic Transport in LiFePO 4 Single Crystals. *Electrochemical and Solid-State Letters* **2007**, *10* (1), 13–16. https://doi.org/10.1149/1.2388240.

(53) Amin, R.; Ravnsbæk, D. B.; Chiang, Y.-M. Characterization of Electronic and Ionic Transport in Li1-xNi0.8Co0.15Al0.05O2(NCA). *Journal of The Electrochemical Society* **2015**, *162* (7), A1163–A1169. https://doi.org/10.1149/2.0171507jes.

(54) Yao, K. P. C.; Okasinski, J. S.; Kalaga, K.; Shkrob, I. A.; Abraham, D. P. Quantifying Lithium Concentration Gradients in the Graphite Electrode of Li-Ion Cells Using: Operando Energy Dispersive X-Ray Diffraction. *Energy and Environmental Science* **2019**, *12* (2), 656–665. https://doi.org/10.1039/c8ee02373e.

(55) Li, Y.; Weker, J. N.; Gent, W. E.; Mueller, D. N.; Lim, J.; Cogswell, D. A.; Tyliszczak, T.; Chueh, W. C. Dichotomy in the Lithiation Pathway of Ellipsoidal and Platelet LiFePO4 Particles Revealed through Nanoscale Operando State-of-Charge Imaging. *Advanced Functional Materials* **2015**, *25* (24), 3677–3687. https://doi.org/10.1002/adfm.201500286.

(56) Steinrück, H. G.; Takacs, C. J.; Kim, H. K.; MacKanic, D. G.; Holladay, B.; Cao, C.; Narayanan, S.; Dufresne, E. M.; Chushkin, Y.; Ruta, B.; Zontone, F.; Will, J.; Borodin, O.; Sinha, S. K.; Srinivasan, V.; Toney, M. F. Concentration and Velocity Profiles in a Polymeric Lithium-Ion Battery Electrolyte. *Energy and Environmental Science* **2020**, *13* (11), 4312–4321. https://doi.org/10.1039/d0ee02193h.

(57) Riess, I. Review of the Limitation of the Hebb-Wagner Polarization Method for Measuring Partial Conductivities in Mixed Ionic Electronic Conductors. *Solid State Ionics* **1996**, *91* (3), 221–232. https://doi.org/10.1016/S0167-2738(96)83022-0.

(58) Weppner, W.; Huggins, R. A. Determination of the Kinetic Parameters of Mixed-Conducting Electrodes and Application to the System Li3Sb. *Journal of The Electrochemical Society* **1977**, *124* (10), 1569–1578. https://doi.org/10.1149/1.2133112.

(59) Verma, A.; Smith, K.; Santhanagopalan, S.; Abraham, D.; Yao, K. P.; Mukherjee, P. P. Galvanostatic Intermittent Titration and Performance Based Analysis of LiNi 0.5 Co 0.2 Mn 0.3 O 2 Cathode. *Journal of The Electrochemical Society* **2017**, *164* (13), A3380–A3392. https://doi.org/10.1149/2.1701713jes.

(60) Dees, D. W.; Kawauchi, S.; Abraham, D. P.; Prakash, J. Analysis of the Galvanostatic Intermittent Titration Technique (GITT) as Applied to a Lithium-Ion Porous Electrode. *Journal of Power Sources* **2009**, *189* (1), 263–268. https://doi.org/10.1016/j.jpowsour.2008.09.045.

(61) Hebb, M. H. Electrical Conductivity of Silver Sulfide. *The Journal of Chemical Physics* **1952**, *20* (1), 185–190. https://doi.org/10.1063/1.1700165.

(62) Wagner, C. Beitrag Zur Theorie Des Anlaufvorgangs. *Zeitschrift für Physikalische Chemie* **1933**, *21B* (1), 25–41. https://doi.org/doi:10.1515/zpch-1933-2105.

(63) Yokota, I. On the Theory of Mixed Conduction with Special Reference to Conduction in Silver Sulfide Group Semiconductors. *Journal of the Physical Society of Japan* **1961**, *16* (11), 2213–2223. https://doi.org/10.1143/JPSJ.16.2213.

(64) Maier, J. Ionics versus Electronics, and the General Case of Mixed Conductor. *Annalen der Physik* **2006**, *15* (7–8), 469–479. https://doi.org/10.1002/andp.200510201.

(65) Deng, C.; Wang, Y.; Qin, C.; Fu, Y.; Lu, W. Self-Directed Online Machine Learning for Topology Optimization. *Nature Communications* **2022**, *13* (1), 388. https://doi.org/10.1038/s41467-021-27713-7.

(66) Raissi, M.; Perdikaris, P.; Karniadakis, G. E. Physics-Informed Neural Networks: A Deep Learning Framework for Solving Forward and Inverse Problems Involving Nonlinear Partial Differential Equations. *Journal of Computational Physics* **2019**, *378*, 686–707. https://doi.org/10.1016/j.jcp.2018.10.045.

(67) Wu, B.; Zhang, B.; Deng, C.; Lu, W. Physics-Encoded Deep Learning in Identifying Battery Parameters without Direct Knowledge of Ground Truth. *Applied Energy* **2022**, *321*, 119390. https://doi.org/10.1016/j.apenergy.2022.119390.

(68) Peterson, P. F2PY: A Tool for Connecting Fortran and Python Programs. *International Journal of Computational Science and Engineering* **2009**, *4* (4), 296–305.

(69) Lee, K.-C.; Yoo, H.-I. Hebb–Wagner-Type Polarization/Relaxation in the Presence of the Cross Effect between Electronic and Ionic Flows in a Mixed Conductor. *Journal of Physics and Chemistry of Solids* **1999**, *60* (7), 911–927. https://doi.org/10.1016/S0022-3697(99)00002-5.

(70) Riess, I. Analysis of Hebb-Wagner Polarization Measurements under Relatively High Applied Voltages. *Solid State Ionics* **1993**, *66* (3), 331–336. https://doi.org/10.1016/0167-2738(93)90423-Z.

(71) Mistry, A.; Verma, A.; Sripad, S.; Ciez, R.; Sulzer, V.; Brosa Planella, F.; Timms, R.; Zhang, Y.; Kurchin, R.; Dechent, P.; Li, W.; Greenbank, S.; Ahmad, Z.; Krishnamurthy, D.; Fenton, A. M.; Tenny, K.; Patel, P.; Juarez Robles, D.; Gasper, P.; Colclasure, A.; Baskin, A.; Scown, C. D.; Subramanian, V. R.; Khoo, E.; Allu, S.; Howey, D.; DeCaluwe, S.; Roberts, S. A.; Viswanathan, V. A Minimal Information Set To Enable Verifiable Theoretical Battery Research. *ACS Energy Letters* **2021**, *6* (11), 3831–3835. https://doi.org/10.1021/acsenergylett.1c01710.

APPENDICES

Appendix A. Checklist[71] Summarizing Theoretical and Computational Aspects of the Present Study.

Manuscript Title	:	How Machine Learning Can Extend Electroanalytical Measurements Beyond Analytical Interpretation
Submitting Author*	:	Aashutosh Mistry

	Y/N/NA[a]
Q1. Have you provided all assumptions, theory, governing equations, initial and boundary conditions, material properties (e.g., open-circuit potential) with appropriate precision and literature sources, constant states (e.g., temperature), etc.?	Y
Remarks:	
Q2. If the calculations have a probabilistic component (e.g., Monte Carlo, initial configuration in Molecular Dynamics, etc.), did you provide statistics (mean, standard deviation, confidence interval, etc.) from multiple (≥3) runs of a representative case?	Y
Remarks: refer to **Error! Reference source not found.** and **Table 3**.	

Q3. If data-driven calculations are performed (e.g., machine learning), did you specify dataset origin, the rationale behind choosing it, what information it contains, and the specific portion of it being utilized? Have you described the thought process for choosing a specific modeling paradigm?	Y
Remarks: The discussion section describes the rationale for choosing Bayesian Optimization.	
Q4. Have you discussed all sources of potential uncertainty, variability, and errors in the modeling results and their impact on quantitative results and qualitative trends? Have you discussed the sensitivity of modeling (and numerical) inputs such as material properties, time step, domain size, neural network architecture, etc. where they are variable or uncertain?	Y
Remarks:	
Q5. Have you sufficiently discussed new or not widely familiar terminology and descriptors for clarity? Did you use these terms in their appropriate context to avoid misinterpretation? Enumerate these terms in the "Remarks".	Y
Remarks: no new terminology has been introduced; Newman number, $\mathbb{Ne}$, is not widely familiar and its mathematical expression along with appropriate references defining it have been cited	

* I verify that this form is completed accurately in agreement with all co-authors, to the best of my knowledge.

[a] Y ≡ the question is answered complete. Discuss any N or NA responses in "Remarks".

Appendix B. Nomenclature.

symbol	description
$\mathcal{A}$	acquisition function, refer to Eq. [8]
C_i	interfacial capacitance [μF/cm^2]
c	concentration [mol/m^3]
$\tilde{c}$	scaled concentration, *unitless*, refer to Eq. [19]
$\mathcal{D}$	chemical diffusivity [cm^2/s]
F	Faraday's constant [96487 C/mol]
$f_{\text{M}\Theta}$	activity coefficient, *unitless*
i	current density [mA/cm^2]
L	pellet thickness [mm]
N	number of initial guesses, samples, time points, etc.
$\mathbb{Ne}$	Newman number, *unitless*
R	Universal gas constant [8.314 J/mol·K]
R_i	interfacial resistance [Ω·cm^2]
T	temperature [K]
t	time [1 min ≡ 60 s]
t_+^Θ	transference number of Mg^{2+} filled sites relative to empty sites, *unitless*
v_Θ	continuum velocity of empty sites [m/s]
x	spatial coordinate [1 m ≡ 10^2 cm ≡ 10^3 mm]

Greek symbols:

α	proportionality constant in Eq. [2]
Δ	difference function for a given choice of material properties; defined by Eq. [6]
ξ	parameter in $\mathcal{A}$
σ	total conductivity [S/cm], (also) standard deviation
τ	time constant in Eq. [1]
ϕ	potential [V]

Superscripts/ subscripts:

eq	equilibrium
i	interface
max	maximum
0	value at $x = 0$
$\mathcal{D}$	related to chemical diffusivity, $\mathcal{D}$
L	value at $x = L$
$R_\text{i}C_\text{i}$	related to interfacial resistance, R_i, and capacitance, C_i
Θ	empty sites

Abbreviations:

RMS	root mean squared